JOURNAL OF PROPULSION AND POWER
Vol. 16, No. 5, September–October 2000

Unsteady Viscous Flow Causing Rotor-Stator Interaction in Turbines, Part 1: Data, Code Pressure

B. Lakshminarayana,* A. Chernobrovkin,† and D. Ristic†
Pennsylvania State University, University Park, Pennsylvania 16802

A coupled experimental and computational study of the effects of the nozzle wake-rotor interaction is carried out to understand the cause and effects of the unsteady flow in turbine rotors. The paper is organized in two parts. Part 1 deals with the experimental and numerical program and interpretation of the blade pressure field. The experiment was carried out in a low-speed turbine at 22.6% of the nozzle chord spacing between the rotor and the nozzle. The laser Doppler velocimetry (LDV) data, acquired earlier, is integrated with the dynamic pressure measurements and numerical simulation to provide an integrated interpretation. A systematic study has been carried out to evaluate the effect of the turbulence model and artificial dissipation on the accuracy of the numerical prediction. The steady flowfield, unsteady pressure at design and off-design conditions on both blade surfaces, and the hub are presented, interpreted, and compared with the predictions from the Navier–Stokes code. The predictions are in a good agreement with the data. The second part deals with the integrated interpretation of the unsteady velocity and pressure field, as well as the flow physics associated with the nozzle wake transport and decay.

Nomenclature

C_f = skin-friction coefficient, $\tau_w/(\rho_1 \bar{W}_1^2)$
C_p = pressure coefficient, $(p - \bar{p}_1)/(\rho_1 \bar{W}_1^2/2)$
C'_p = pressure coefficient, $(p - \bar{p}_2)/(\rho_1 \bar{W}_{x1}^2/2)$
C_{pi} = ith harmonic of C_p
C_{p0} = total pressure coefficient, $(P_0 - \bar{P}_{01})/(\rho_1 \bar{W}_1^2/2)$
C_x = rotor axial chord length
i = incidence angle
k = turbulent kinetic energy
k_4 = coefficient of the fourth-order artificial dissipation
P = turbulent kinetic energy production
P_s = pressure surface
P_0 = total pressure
p = static pressure
Re = Reynolds number based on chord
R_{ij} = rotation rate tensor
S = rotor blade spacing
S_{ij} = strain rate tensor
S_n = vane spacing
S_1 = local passage width (rotor)
T = period
Tu = turbulence intensity based on inlet total relative velocity
t = physical time
U_m = rotational velocity at midspan
u_τ = friction velocity
V = absolute total velocity
W = total relative velocity
x = axial length measured from rotor leading edge
y = distance in pitchwise direction
y^+ = inner variable, $u_\tau y/\nu$
α = absolute flow angle
β = relative flow angle
ΔC_p = $C_p - C_{p_{av}}$
μ_t = eddy viscosity coefficient
ν = kinematic viscosity
τ = pseudotime
τ_w = wall shear stress
ω = wake passing frequency
Ω = reduced frequency, $\omega C_x / V_{x0}$

Subscripts

av = time average
t = turbulent
x = axial
0 = inlet to the nozzle, freestream
1 = rotor inlet
2 = rotor outlet

Superscripts

$\sim$ = ensemble average
$'$ = unresolved unsteadiness
$-$ = time average

Introduction

THE flowfield in a turbine rotor is unsteady. The unsteadiness, caused by relative motion between a stator (or vane) blade and a rotor blade, has a major influence on the aerodynamic, mechanical, and thermal performance as well as the cooling requirements for turbines. The mechanical reliability, life, and cycle performance are all substantially altered because of these interactions. The unsteadiness is caused by several phenomena; the potential (pressure) interaction between a rotor and a stator, the viscous interaction caused by velocity and pressure gradients in blade/vane wakes impinging on a subsequent blade row, the random unsteadiness in the freestream, and the unsteadiness caused by the interaction of endwall flows (secondary and leakage flows) with the subsequent blade row.

There have been many attempts in recent years to investigate such flows computationally (e.g., Refs. 1 and 2). The Navier–Stokes/Euler procedure will be used extensively in the future to achieve high performance and a reduced number of stages through accurate simulation of the flowfield through a parametric variation of operating conditions and variables. More importantly, these models are based upon fundamental fluid mechanics allowing the designer to investigate analytically component design features outside the

Presented as Paper 98-3595 at the AIAA/ASME/SAE/ASEE 34th Joint Propulsion Conference, Cleveland, OH, 13–15 July 1998; received 14 August 1998; revision received 21 June 1999; accepted for publication 28 June 1999.

*Evan Pugh Professor, Director of Center for Gas Turbine and Power, Department of Aerospace Engineering. Fellow AIAA.

†Research Assistant, Department of Aerospace Engineering. Member AIAA.

empirical database. As component design tools, these models will have a significant impact on the design of future turbines.

Four groups have measured the unsteady flowfield inside a turbine rotor; the groups at UTRC,[3] Cambridge,[4] Calspan,[5] and DFVLR.[6] There is a further need for flowfield measurements in a turbine rotor with realistic nozzle-rotor spacing that will include both the potential flow and wake interactions. One of the objectives of this research is to accomplish this task.

The coupled experimental and computation study, which is more comprehensive than hitherto attempted, should provide a detailed understanding of the flow physics. Almost all earlier experimentalists have concentrated their effort on blade surface measurements (e.g., pressure, skin friction, and transition). The present approach is to derive information on both the velocity field and the blade surface properties caused by rotor-stator interaction. Likewise, the computational approach involves developing a two-dimensional unsteady Navier–Stokes code, incorporating the transition and turbulence models to predict the nozzle wake, unsteady rotor blade boundary layers, unsteady freestream flowfield, and the blade pressures accurately, and carrying out a simulation study to understand the sources of unsteady viscous flow through turbomachinery stages, including its effects on transition and aerothermodynamic losses.

Because this is an integrated computational-experimental study, no attempt is made to segregate the two. The experimental study in a low-speed turbine is combined with the computational results to develop new insight into flow physics. The first part of this paper includes the computational and experimental techniques and the pressure field. A detailed study of the flowfield and integrated interpretation of the results are given in Part 2 of the paper.

Experimental Program

The Axial Flow Turbine Research Facility (AFTRF) of The Pennsylvania State University is an open circuit facility 0.9166 m (3 ft) in diameter and a hub-to-tip radius ratio of 0.73, with an advanced axial turbine blading configuration (Fig. 1). There are 23 nozzle guide vanes and 29 rotor blades followed by outlet guide vanes. A window for laser Doppler velocimetry (LDV) measurements covering the entire flow field from upstream of the nozzle to downstream of the rotor passage is also incorporated. Detailed design of the facility, performance, and geometric features are described in Ref. 7. Blade coordinates can be downloaded from the Web site (turbo S.aero.psu.edu). Some important performance and geometric parameters are as follows: hub/tip ratio = 0.7269; nozzle, axial chord (midspan) = 11.23 cm, turning angle = 70 deg; rotor, axial blade chord (midspan) = 9.294 cm, turning angle = 95.42 deg at tip, and 125.69 deg at root; tip clearance = 0.97 mm; Reynolds number of nozzle flow (based on exit flow) = 10^6; mass-flow rate = 11.05 kg/s; loading coefficient ($2\Delta P_0/\rho U_m^2$) = 3.88; and rotational speed = 1330 rpm. The vane-blade spacing is 22.6% of the nozzle axial chord at the midspan. The design velocity triangles at the inlet and exit of the rotor are shown in Fig. 1.

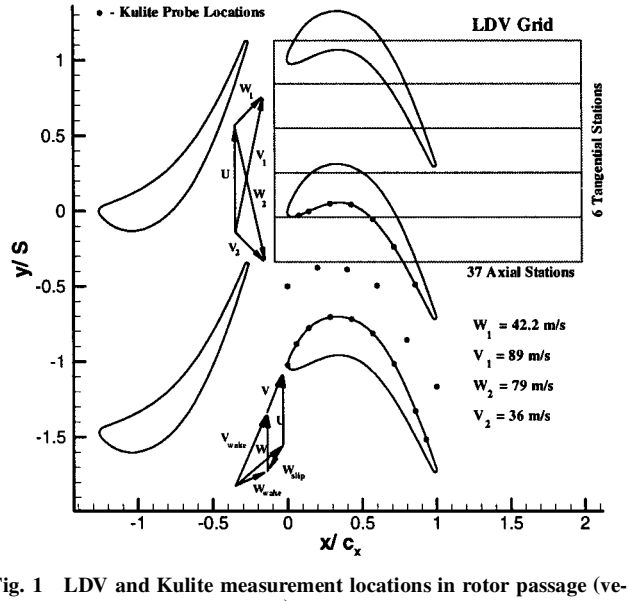

Fig. 1 LDV and Kulite measurement locations in rotor passage (velocity triangle is based on design).

Comprehensive data were acquired within and downstream of the nozzle during the earlier phase of the research program. A complete five-hole probe survey was carried out at 2.5 and 9% nozzle chord downstream of the nozzle trailing edge.[8] Furthermore, LDV measurements carried out at midspan of the rotor (upstream to downstream) establish the details of distortion and nozzle wake profile upstream of the rotor.[9] Hence all of the rotor inflow properties (time dependent in rotor frame) are known and shown in Fig. 2.

The LDV measurements at the rotor midspan are carried out at the design condition (Table 1). The blade dynamic pressure data at midspan and hub are acquired at design and three off-design conditions, and these are shown in Table 1. This was achieved by varying the turbine speed and the mass flow. The off-design data listed in Table 1 are based on one-dimensional consideration. The upstream flowfield was not acquired at the off-design conditions. The inlet

Table 1 Operating conditions

	Design	Off-design		
Operating conditions	A	B	C	D
Mass flow, kg/s	10.42	10.42	5.82	5.82
RPM	1330	1235	1100	800
V_x, ms	30.43	30.43	16.8	16.8
U_m, ms	55.32	51.35	45.75	33.27
Rotor inlet flow angle (β_1) in degree	41.44	45.76	−4.75	33.4
Incidence, deg	−1.9	2.06	−44.9	−7.6
$\Omega = \omega C_x / V_x$	4.89	4.54	7.32	5.82
Re	2.15×10^5	2.15×10^5	1.19×10^5	1.19×10^5

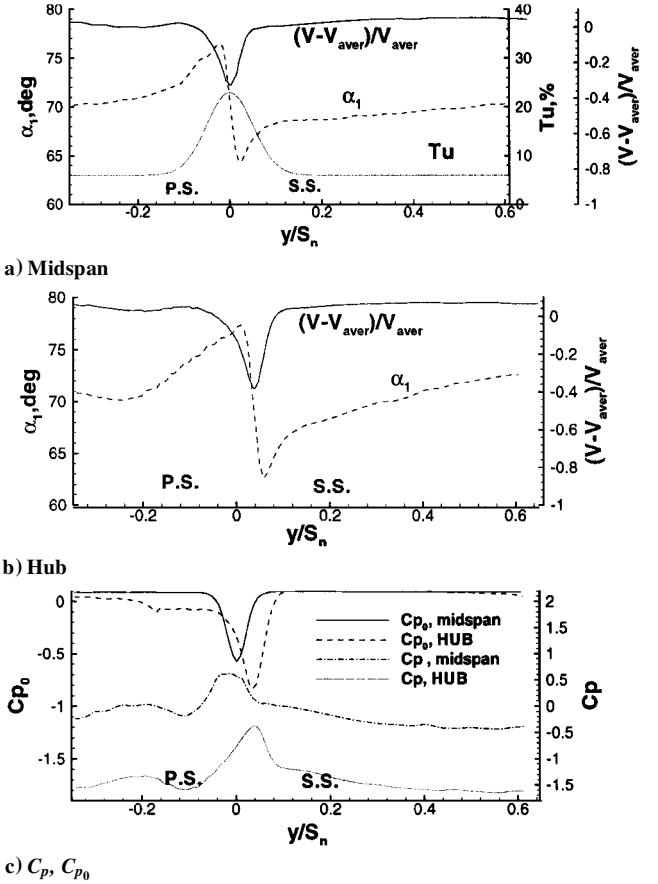

Fig. 2 Variation of rotor inlet static and stagnation pressure coefficients, velocity and turbulence quantities at $x/C_x = -0.244$ and design conditions (case A).

flow properties ($x/C_x = -0.224$) are shown in Fig. 2 at midspan ($H = 0.5$) of the rotor and near the hub ($H = 0.035$). These are also the inlet conditions used for the computation. It is clear that substantial velocity, flow angle, stagnation, and static pressure gradients exist in the nozzle wake, both at the hub and the midspan regions. Most of the earlier research was carried out at larger nozzle-rotor spacing, where the pressure wakes do not exist as they decay rapidly downstream. The present measurement is carried out at practical spacing; and hence, all of the features of modern turbines are present, including both the pressure and velocity gusts because of the viscous wakes.

The reduced frequency based on the upstream nozzle wake frequency, rotor axial chord, and axial velocity upstream of nozzle varies from 4.54 to 7.32. Because there are significant differences between the condition A (design) and C (off design), only the data at these two conditions are presented and interpreted.

Laser Doppler Velocimeter Data

Detailed steady and unsteady flow data were acquired at the midspan of the rotor blade using a two-dimensional LDV. The measurements were carried out at 37 axial locations upstream of the rotor ($x/C_x = -0.088$) to one chord downstream of the rotor.[9] To account for the nonuniformity of the rotor absolute inlet flowfield, measurements were made at six tangential locations in the absolute frame equally spaced over one nozzle pitch (Fig. 1). These six tangential positions represent six different relative positions between the nozzle and the rotor (labeled positions 1 through 6) or if viewed from the nozzle frame of reference, six different time-resolved positions of the rotor in relation to the nozzle.

At each survey point approximately 120,000 velocity measurements were acquired. Because all of the velocity components were spatially phase-lock averaged, which results in a representative rotor passage with 50 measurement windows, there were 2400 velocity measurements on average in each measurement window. After all instantaneous velocity measurements were acquired for each particular survey point, the velocity is then ensemble-averaged at each measurement window.

The instantaneous velocity V_i is decomposed as follows:

$$V_i = \bar{V} + \tilde{V} + V' \tag{1}$$

where $\bar{V}$ is the time-averaged velocity, $\tilde{V}$ is the periodic velocity, and V' is the unresolved velocity.

The variance is given by

$$\overline{(V')^2} = \left[\sum_{i=1}^{n} (V_i - \tilde{V}\bar{V})^2\right]/(n-1) \tag{2}$$

The level of unresolved unsteadiness in each measurement window is determined by the variance.

The cycle-averaged values are obtained by averaging the ensemble-averaged (and phase-lock averaged) properties in each rotor measurement window for one nozzle/rotor location over the six nozzle/rotor locations (see Fig. 1).

The experimental procedure and data processing are designed to obtain spatial and temporal measurements (i.e., rotor shaft positions; not real time) of the wake-rotor interaction generated unsteadiness in the rotor. The laser is located at a fixed position relative to the nozzle wake for each nozzle/rotor location. Hence, the averaging is based on identical rotor-nozzle blade positions. These measurements are similar to those reported by earlier investigators.[10]

A complete error analysis for these measurements is given by Zaccaria.[11] Based on this error analysis, the uncertainty for a 95% confidence level is as follows: outside the rotor wake 0.4 and 2.8%, respectively, for the ensemble-averaged velocity and the unresolved component of velocity; inside the rotor wake, 4.0 and 14.8% for the ensemble-averaged and unresolved velocity, respectively. The LDV data are presented and interpreted by Zaccaria and Lakshminarayana.[9] These data are used in Part 2 of this paper to validate the code and to derive new insight on the nozzle-rotor viscous interaction in view of the additional blade surface data acquired recently and the comprehensive flow simulation carried out with an unsteady Navier–Stokes code.

Dynamic Pressure Measurements

The implementation of the dynamic pressure transducers in the turbine rig was driven by space limitations. The pressure transducers are inserted into chambers, which in turn are connected to the turbine airfoil surfaces through 0.5–0.8-mm-diam holes. The design objective is to achieve a frequency response of 40 kHz. The miniature sensors used are the Kulite model XCS-093 with a pressure range of maximum 5 psia. They are capable of measuring pressure fluctuations to an accuracy of 0.01 psia. A schematic showing the location of dynamic pressure transducers on the blade at midspan (16) and on the hub (endwall) surface (5) is shown in Fig. 1. The low-level signals from the dynamic pressure transducers are amplified in the rotating frame by using miniature amplifiers. The amplifiers rotate in the rotor frame and provide a high-level signal output before the signal reaches the slip-ring unit. The transducers were calibrated by inserting the entire blade in a pressure chamber as well as using the steady-state static pressures on the blade before the experiment.

The dynamic pressure data from the rotor are transmitted through the rotating drum to a slip-ring unit. The slip-ring unit is of the brush type and has 150 channels. The slip-ring unit is housed in a cowling in front of the facility. Each ring carries four brushes made of silver graphite. The rings are made up of coin silver, which withstands up to current levels of 5 A. The brushes are individually removable and replaceable. The contact resistance is about 5 mΩ maximum.

A completely automated data processing system is built around a computer with a clock rate of 7 MHz. The data are triggered by an encoder on the turbine shaft. Approximately 167 (1 million samples at 6000 samples/rev.) revolutions of data are acquired. This was ensemble-averaged to derive revolution periodic, which is then decomposed into blade periodic (average-passage) and blade aperiodic pressures. The procedure used for data processing is similar to that described in the last section. The latter represents the deviation of the individual passage from the average passage. A typical set of processed data for $x/C_x = 0.285$ is shown in Fig. 3. The blade aperiodic quantity is small for most passages and appreciable only in three or four passages. Only the blade periodic data are presented and interpreted in this paper.

Numerical Procedure

Technique and Models

An explicit four-stage Runge–Kutta scheme is used for the time integration of both averaged mean and turbulence equations. A fourth-order artificial dissipation is included to damp high wave-number errors, and a second-order dissipation is used to improve the shock capturing. Eigenvalue and velocity scaling are used to optimize the amount of the artificial dissipation. Multigrid and implicit residual smoothing are used to improve the convergence characteristics of the steady solver. Nonreflecting boundary conditions are incorporated to minimize the reflection at boundaries and to minimize the computational domain. The steady Navier–Stokes solver[12,13] has been modified to enable a time-accurate solution. The basic code has been extended to include the pseudo-time inner iteration. This approach resulted in a major acceleration of the unsteady code. Details

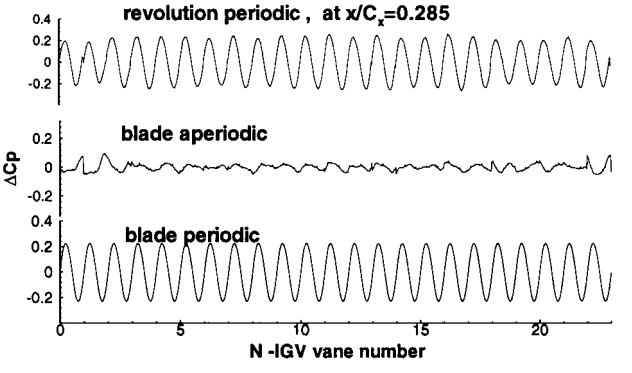

Fig. 3 Decomposition of the revolution periodic data into blade periodic (average passage) and blade aperiodic.

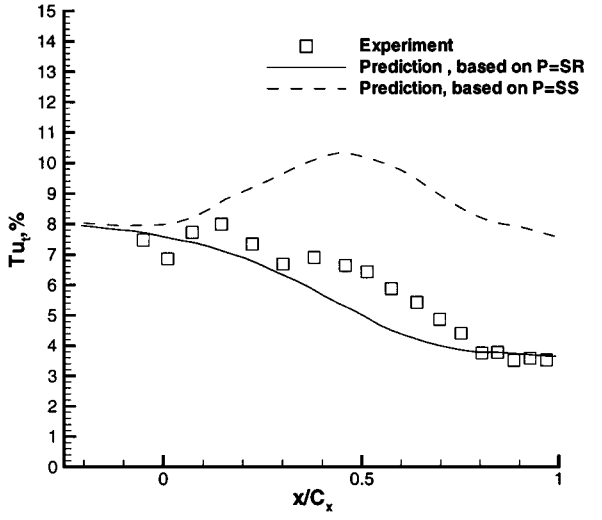

Fig. 4 Turbulence intensity at midpitch inside the rotor passage.

of the pseudotime scheme and the validation of the unsteady solver can be found in Ref. 14. A set of low-Reynolds-number k–ε turbulence models are utilized for turbulence closure. Based on the preceding assessment of the turbulence models suitable for the transitional flow, the Fan–Lakshminarayana–Barnett turbulence model[15] has been chosen for the current research.

A comparison of the predicted turbulence field with experimental results (Fig. 4) shows that the simulation based on the original k–ε model overpredicts the level of the freestream turbulence beyond $x/C_x = 20\%$. The turbulence production caused by a large strain in this region is not compensated by an increase in the turbulence dissipation rate. Replacement of the turbulence production term based on the rate of the deformation tensor, $P = 2\nu_t \sqrt{[(S_{ij})^2 \cdot (S_{ij})^2]}$ [denoted as (SS)] with $P = 2\nu_t \sqrt{[(S_{ij})^2 \cdot (R_{ij})^2]}$ (denoted as SR), led to the improved prediction of the freestream turbulence field (Fig. 4). This modification does not affect the nozzle wake region. In the nozzle wake $(S_{ij})^2$ is approximately equal to the $(R_{ij})^2$. Therefore, this modification does not affect the nozzle wake propagation through the cascade.

To simulate rotor unsteady flow, time-dependent boundary conditions were imposed at rotor inlet. Velocity and the pressure distributions were based on the experimental data at 24.59% of the rotor chord upstream of the leading edge. Data were obtained using a five-hole probe in a stationary frame of reference. To impose an accurate unsteady boundary condition, the measured pressure and velocity fields (moving in rotor frame of reference) were superposed with the rotor potential field based on a steady prediction (steady in the rotor frame of reference).

To apply periodic boundary conditions, the flow in five rotor passages was calculated. This provides a vane-to-blade ratio equal to 4:5, close to the actual ratio of 23:29. All computational results presented in this paper and in Part 2 are based on a two-dimensional simulation.

Sensitivity Studies

This code has been validated for a wide variety of steady and unsteady flows.[14] Hence, only the sensitivity study is reported for this particular case.

To analyze the grid sensitivity, numerical simulations were carried out using three grids: 101 × 61, 181 × 91, and 211 × 181 (a figure with the grid topology can be downloaded from the Web site). The distance between the first grid point and the wall varied from $y^+ = 0.9$ for the coarse grid to $y^+ = 0.3$ for the fine grid. Steady flow predictions based on 181 × 91 and 211 × 181 grids were identical. A numerical simulation of the unsteady flow imposes an additional requirement on the grid density outside the boundary layer. An earlier analysis of the influence of artificial dissipation[14] has been used to estimate the required mesh distribution in the middle of the passage. The axial gap in the turbine stage is equal to 27.6% of the rotor chord. Hence, the nozzle wake defects are substantial. At least 10 Fourier harmonics are needed for an accurate representation of the inlet velocity field. The amplitude of the tenth harmonic is 2% of the wake defect. According to the preceding analysis, the finest grid (211 × 181) provides enough spatial resolution to model the whole spectrum of the inlet wake. A numerical simulation based on 181 × 91 grid may lead to excessive decay of the eighth and higher harmonics because of the artificial dissipation. A comparison of the numerical prediction of the unsteady flow based on these two grids indicates that utilization of the coarser grid (181 × 91) results in a 3% smaller local wake defect because of the artificial dissipation. No other significant differences were observed. To minimize CPU time, most of the simulation studies were carried out using a 181 × 91 grid.

The accuracy of the numerical simulation depends on the appropriate choice of the number of physical time steps as well as the number of inner pseudotime steps. Current simulations were carried out with 1000 physical time steps per period. Even though it was found that 500 time steps were enough for the accurate temporal resolution, the solution had features of numerical instability. This problem was eliminated when the number of physical time steps was increased to 1000. An investigation of the dependency of the solution on the number of inner iterations indicated that accurate prediction of the unsteady pressure field required about seven inner iterations. An accurate resolution of the velocity and turbulence field required 15 inner iterations.

One of the objectives of the current research is to evaluate the ability of the code to predict unsteady transitional flows in a turbine. Current computations are carried out without the incorporation of a transitional model. The k–ε model represents the complex nonlinear physics of the transitional process in the boundary layer through a combination of the diffusion of the freestream turbulence and the local balance between the turbulence production and the dissipation. The k–ε field is transformed from one semistable condition (laminar) to another semistable condition (turbulent). The flow in the transitional region is most sensitive to the numerical aspect of the solver. In addition to the quality of the particular low Re turbulence model, the level of the artificial dissipation plays a crucial role in the prediction of the transition region. Artificial dissipation depends on the local properties of the grid and the coefficient k_4. As just stated, prediction is grid independent for both fine grids. The location of the transition and the skin-friction coefficient beyond transition strongly depends on the value of k_4 (presented in the original paper[16]). An excessive level of the artificial dissipation leads to laminarization of the boundary layer. An increase in k_4 results in the transition onset shifting from $x/C_x = 0.65$ to the trailing edge on the suction surface. The essential feature of the current solver is that for the calculations with $k_4 < 0.015$; the transition prediction is found to be independent of the level of the artificial dissipation coefficient. This value of the k_4 coefficient is found to be universal for other configurations (flat plate, compressor cascade, low-pressure turbine), under the condition that the solution is grid independent.

Time-Averaged Flowfield

A comparison between the predicted (steady) and measured surface pressure distribution is shown in Fig. 5 for the design condition. The comparison for off-design conditions are shown in Ref. 16. The comparison is done for four cases (summarized in Table 1). Very good agreement between the predicted and the experimental data is achieved for the design point (Fig. 5) as well as for the flows with moderate incidence angle. A comparison of the blade surface pressure distribution at different operating conditions indicates that the flow is not sensitive to the moderate variation in the incidence angle and the prediction is excellent at these conditions. The predicted (time-averaged) and measured (cycle-averaged) relative total velocity distribution at several axial locations at design condition (A) are shown in Fig. 6. The prediction is excellent at all locations except at $x/C_x = 110\%$. One of the severest tests on the code is the ability to capture a large gradient in velocity. Near the leading edge, the excellent agreement at $x/C_x = -5\%$ provides confidence in the code.

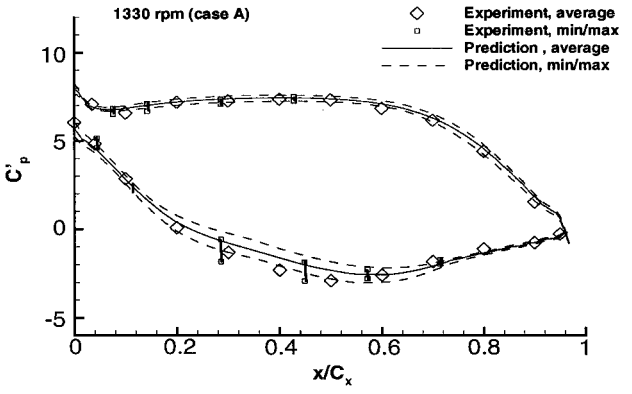

Fig. 5 Average blade pressure and unsteady pressure envelope at design conditions (midspan).

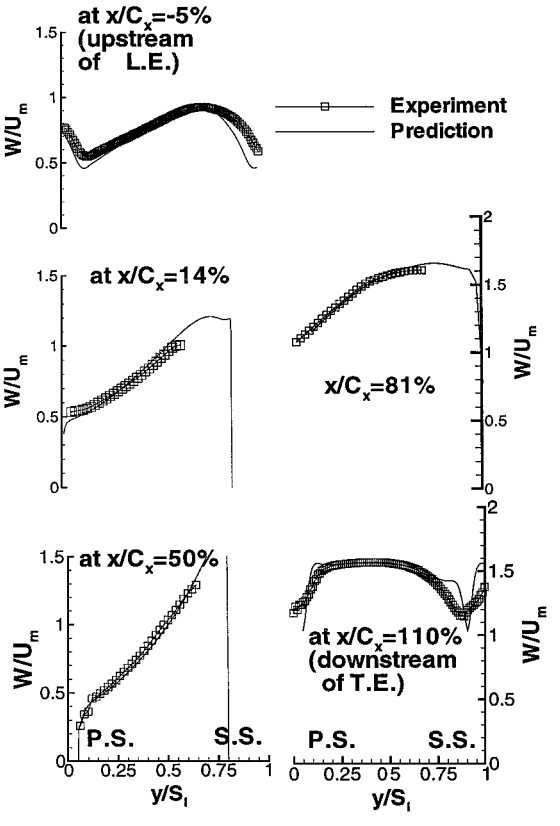

Fig. 6 Blade-to-blade distribution of relative velocity.

The wake depth is captured at $x/C_x = 110\%$, but the predicted wake width is smaller than the measured one. This may be attributed to the three-dimensional effects or the cycle-averaging procedure. The predicted passage average angle at the exit is 67.4 deg. This compares well with the measured and design values of 64.3 and 67 deg, respectively. These results indicate that the time-averaged flowfield is predicted accurately especially in the passage and upstream of the passage.

Unsteady Pressure Field on the Blade Surface

Before commenting on the nature and magnitude of unsteady pressure, we note that the blading for the Penn State high-pressure turbine was designed to limit overacceleration on the suction surface just off of the leading edge.[7] On any turbine blade the flow is subject to high acceleration around the leading-edge region on both the suction and the pressure sides. In both cases there may be a subsequent undesirable diffusion, although a local diffusion, however small, is of more concern on the suction side, where it may constitute a significant disturbance to the (laminar) boundary layer. In the present blading design it was possible to trade one off against the other by precise tailoring of the leading-edge geometry and adjustment to the leading-edge inclination (i.e., incidence). Generally, only a very slight tendency to overspeed was tolerated on the suction surface because a very minor increase in the pressure surface diffusion would not significantly affect the blade performance. The suction peak is located near the midchord location.

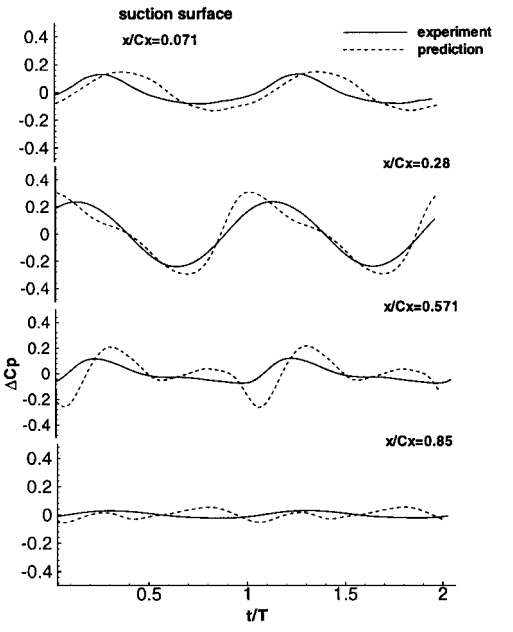

Fig. 7 Measured and predicted time history of unsteady pressures on the suction surface (design condition).

The measured and predicted steady pressure and unsteady envelope at the design condition as well as steady pressures are plotted in Fig. 5. The predicted amplitude of unsteady pressures agrees quite well with the measured values. The amplitudes are small near the leading edge on both surfaces because the blading is not very sensitive to incidence changes because of inherent design. The incidence angle changes (Table 1) from 2.06 to −7.6 deg had no significant impact on the steady pressures. The maximum amplitude occurs near 28% chord on the suction surfaces and decreases gradually to insignificant values as the trailing edge is approached (Fig. 5). There is a significant difference between these data and those of Ref. 3, who observed maximum values at the leading edge. This may be caused by large flow acceleration near the leading edge and closer rotor-stator spacing employed by Dring and Joslyn.[3] The amplitudes (Fig. 5) are small on the pressure surface and once again decrease gradually to small values as the trailing edge is approached.

The periodic variation of blade pressures on the suction surface at selected rotor chord locations are shown and compared with the predictions in Fig. 7. As mentioned earlier, the amplitudes are highest near the $x/C_x = 0.28$ and decreases to insignificant values near the trailing edge. The prediction is very accurate at $x/C_x = 0.071$ and 0.28. Discrepancies are observed aft of the midchord. The measurement shows larger decay in the amplitude than the prediction.

The space-time distribution of unsteady pressures (ΔC_p) on both surfaces along all measurement locations are shown in Fig. 8. Such plots can provide a valuable overview of the flow physics associated with the wake-rotor interactions. On the suction surface the measurement shows a maximum value at about 28% of the chord. The phase angle of the peak values (marked HS) on the suction side changes rapidly as the flow progresses downstream because of large changes in the convection velocity of the nozzle wake. The first low value on the suction side (LS1) also moves at about the same phase as the peak (HS). But the second minimum (LS2) is nearly at constant phase. This is much clearer in the contour plots shown in Part 2 of the paper. On the other hand, the peak values on the pressure side occur near the leading edge. One of the unusual features is the presence of two peaks (HP1, HP2) on the pressure side. As indicated earlier and in Fig. 2, the inflow has both the pressure gust

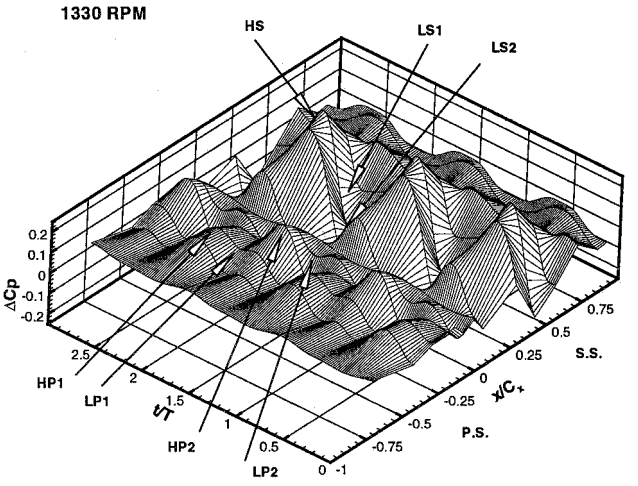

Fig. 8 Measured space-time distribution of blade unsteady pressure, case A (design).

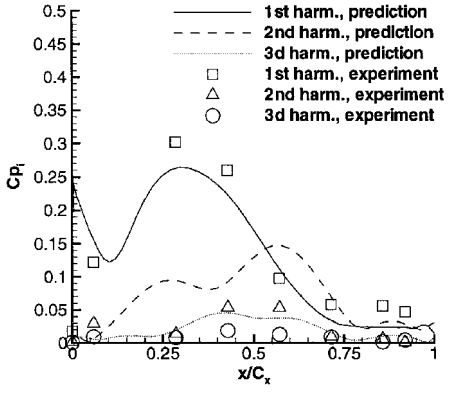

Fig. 9 Measured and predicted harmonics of blade unsteady pressure suction surface.

and the velocity gust. As the two approach the leading edge, the phase angle between the two distortions change, and the pressure gust seems to have a more profound effect on the pressure surface than on the suction side. More details on these features are given in Part 2. Another interesting feature is that, except for the leading edge, the peaks move at nearly constant phase as the flow progresses downstream along the pressure surface. Some of these features are similar to those observed by Dring et al.,[3] but major differences are in the location of peaks on the suction side because of the differences in the blading design.

The first three harmonics of the unsteady pressure on the suction surface are plotted and compared with the predictions in Fig. 9. The experimental data indicate that the first harmonic is the dominant component, and this component is predicted quite well by the code. The predictions reveal two maxima, one near the leading edge and the other near 28% chord downstream. Because there are no data available at the leading edge, the presence of the first peak cannot be confirmed. But the minima observed near the 5% chord location is predicted accurately. The second harmonic shows a peak close to the 50% chord, but the predicted peak is further downstream. The occurrence of the peak in second harmonic can be attributed to the transfer of energy from the first harmonic to the second harmonic in the freestream unsteadiness, which is clear from the fact that the first harmonic decreases rapidly near the midchord and the peak in the second harmonic appears at this location. This is due to the dominant effect of two counter-rotating vortices (see Part 2) that are developed on either side of the wake and the weaker nozzle wake effect. This effect is overpredicted by the code. During the numerical simulations, the observation was made that the amplitude of the second harmonic is sensitive to the local wake velocity defect. The measured values of the third harmonic are negligibly small.

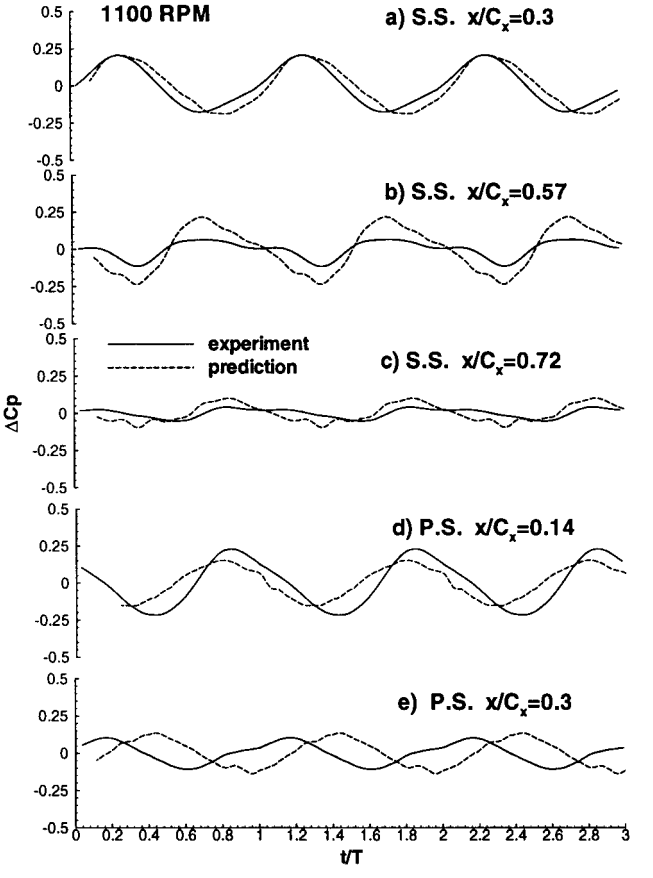

Fig. 10 Measured and predicted time history of unsteady pressure, case C (off design).

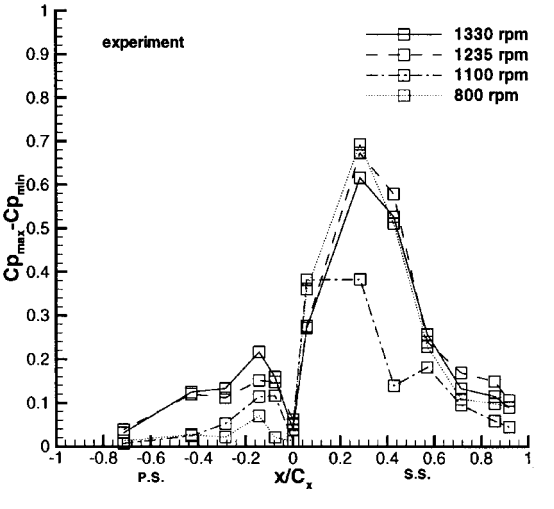

Fig. 11 Maximum variation of surface unsteady pressure, cases A–D.

The measured values at off-design conditions are compared with predictions at selected chordwise locations in Fig. 10. Here again, the agreement is very good near the leading edge, especially on the suction surface. The numerical simulation predicts extended flow separation on the pressure side near the leading edge, which may not be very accurate and may account for the discrepancy in the unsteady pressure distribution at $x/C_x = 0.3$ on the pressure surface.

The chordwise distributions of the unsteady pressure amplitude at all operating conditions (Table 1, cases A, B, C, and D) are shown in Fig. 11. There are two major effects involved here: the time-averaged incidence changes and the reduced frequency changes.

Cases A and B are carried out at the same speed, with case B being at a higher mean incidence. The data on the suction surface show that the amplitudes are slightly higher for case B at most locations. The dominant effect is downstream of the leading edge ($x/C_x = 0.28$ on suction surface, 0.14 on the pressure surface). Cases C and D have the same mass flow and Reynolds number, with case C at more severe off-design condition. The data for case D follow trends very similar to those of cases A and B. As indicated earlier, because of large negative incidence for case C, the peak unsteady pressures are similar on both the suction and the pressure surfaces and have the fastest decay on the pressure side. The amplitudes are highest for this case on the pressure side. One of the interesting features of all of this data is that the peak pressure for all operating conditions (cases A, B, C, and D) occurs downstream of the leading edge on both surfaces. This has a significant impact on the leading-edge cooling. The present design seems to have reduced the unsteady wake-interaction effects near the leading edge through aerodynamic design.

The unsteady pressure on the hub surface is presented and interpreted in the original paper.[16]

Conclusions

The results of an integrated experimental/numerical investigation of the unsteady flow caused by nozzle wake-rotor interaction are presented in this paper. Measured unsteady flowfield and pressure at the midspan and the pressure field on the hub are evaluated and compared with the prediction at the design and off-design condition.

The modification of the production term in the k–ε model is essential for the accurate prediction of the flowfield near the leading edge and in the freestream. The artificial dissipation is found to have a major influence on the accuracy of the predicted inception of transition.

Analysis of the blade unsteady pressure at the design condition reveals the location of the maximum unsteady pressure at $x/C_x = 0.28$. The development of the unsteady pressure on the suction surface is predominantly convective in nature, i.e., the propagation of the pressure spots depends on the local velocity. In contrast, phase pressure variation on the pressure surface indicates an elliptic nature of the wake-blade interaction on the pressure surface.

The high negative incidence angle at off-design condition leads to a significant increase in the unsteady pressure within 15% of the chord downstream of the leading edge on the pressure surface. At the suction surface the peak of the unsteady pressure decays more rapidly in comparison to the design condition.

Good agreement between the predicted and measured data validates the ability of the code to capture the unsteady flow physics. This led to an additional in-depth study of this phenomenon described in Part 2 of the paper.

Acknowledgments

The experimental work was supported by NASA through NAG3-1736 (with R. Boyle and C. Civinskas as technical monitors), and the computational effort was partially supported by NASA Grant NAG3-2025 (with D. Ashpis as technical monitor).

References

[1] Venable, B. L., Delaney, R. A., Busby, J. A., Davis, R. L., Dorney, D. J., Dunn, M. G., Haldeman, C. W., and Abhari, R. S., "Influence of Vane Blade Spacing on Transonic Turbine Stage Aerodynamics, Part 1: Time-Averaged Data and Analysis," American Society of Mechanical Engineers, Paper 98-GT-481, June 1998.

[2] Busby, J. A., Davis, R. L., Dorney, D. J., Dunn, M. G., Haldeman, C. W., Abhari, R. S., Venable, B. L., and Delaney, R. A., "Influence of Vane Blade Spacing on Transonic Turbine Stage Aerodynamics, Part 2: Time Resolved Data and Analysis," American Society of Mechanical Engineers, Paper 98-GT-482, June 1998.

[3] Dring, R. P., Joslyn, H. D., Hardin, L. W., and Wagner, J. H., "Turbine Rotor-Stator Interaction," *Journal of Engineering for Power*, Vol. 104, 1982, pp. 729–742.

[4] Hodson, H. P., "Measurements of Wake Generated Unsteadiness in the Rotor Passages of Axial Flow Turbines," *Journal of Engineering for Gas Turbines and Power*, Vol. 107, No. 2, 1985, p. 468.

[5] Rao, K. V., and Delaney, R. A., "Vane Blade Interaction in a Transonic Turbine," AIAA Papers 92-3323 and 92-3324, Pts. 1 and 2, July 1992.

[6] Arndt, N., "Blade Row Interaction in a Multistage Flow Pressure Turbine," *Journal of Turbomachinery*, Vol. 115, No. 1, 1993, p. 137.

[7] Lakshminarayana, B., Camci, C., Halliwell, I., and Zaccaria, M., "Investigation of Three-Dimensional Flow Field in a Turbine Including Rotor/Stator Interaction, Part 1: Design, Development and Performance of Turbine Facility," AIAA Paper 92-3325, July 1992.

[8] Zaccaria, M., and Lakshminarayana, B., "Investigation of the Three-Dimensional Flow Field at the Exit of a Turbine Nozzle," *Journal of Propulsion and Power*, Vol. 11, No. 1, 1995, pp. 55–63.

[9] Zaccaria, M., and Lakshminarayana, B., "Unsteady Flow Field due to the Nozzle Wake Interaction with the Rotor in Axial Turbine.: Part I -Rotor Passage Flow Field," *Journal of Turbomachinery*, Vol. 119, No. 2, 1997, pp. 201–224.

[10] Hathaway, M., "Unsteady Flows in a Single-Stage Transonic Axial Flow Fan Rotor," NASA TM 88929, Dec. 1986.

[11] Zaccaria, M., and Lakshminarayana, B., "An Experimental Investigation of Steady and Unsteady Flow Fields in Axial Flow Turbines," NASA CR 4778, May 1997.

[12] Fan, S., and Lakshminarayana, B., " Time Accurate Euler Simulation of Interaction of Nozzle Wake and Secondary Flow in an Axial Turbine Stage Using Non-Reflecting Boundary Conditions," *Journal of Turbomachinery*, Vol. 118, No. 4, 1996, pp. 663–678.

[13] Kunz, R., and Lakshminarayana, B., "Three-Dimensional Navier–Stokes Computations of Turbomachinery Flows Using an Explicit Numerical Procedure and a Coupled k-ε Turbulence Model," *Journal of Turbomachinery*, Vol. 114, No. 3, 1992, p. 627.

[14] Chernobrovkin, A., and Lakshminarayana, B., "Development and Validation of Navier–Stokes Procedure for Turbomachinery Unsteady Flow," *AIAA Journal*, Vol. 37, No. 5, 1999, pp. 557–563.

[15] Fan, S., Lakshminarayana, B., and Barnett, M., "Low-Reynolds-Number k-ε Model for Unsteady Turbulent Boundary-Layer Flows," *AIAA Journal*, Vol. 31, No. 10, 1993, pp. 1777–1784.

[16] Lakshminarayana, B., Chernobrovkin, A., and Ristic, D., "Experimental and Numerical Study of Unsteady Viscous Flow due to Rotor Stator Interaction in Turbines. Part 1: Data, Code, and Pressure Field," AIAA Paper 98-3595, July 1998.